

SUPPORTING INFORMATION

XRD patterns of Co-based metal glycerate nanospheres before and after “water treatment”

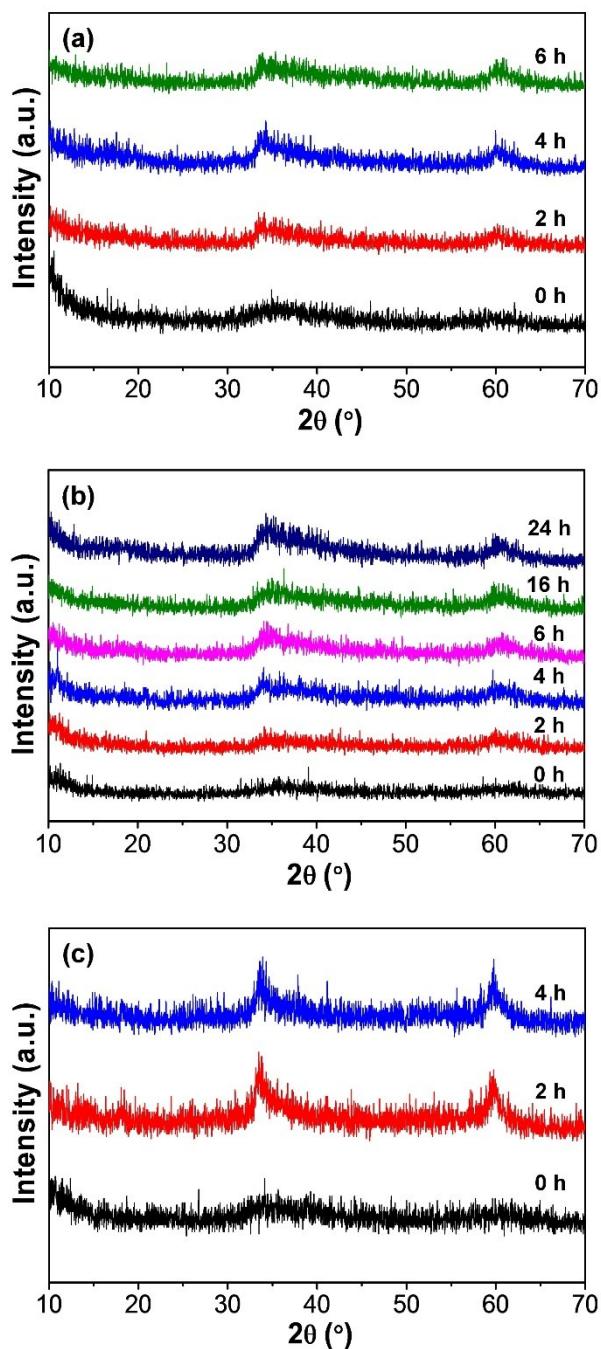


Fig. S1. XRD patterns of (a) Co glycerate, (b) Ni-Co glycerate, and (c) Zn-Co glycerate nanospheres with increasing “water treatment” time.

SUPPORTING INFORMATION

SEM and TEM images of the metal cobaltite ($M\text{Co}_2\text{O}_4$) nanospheres

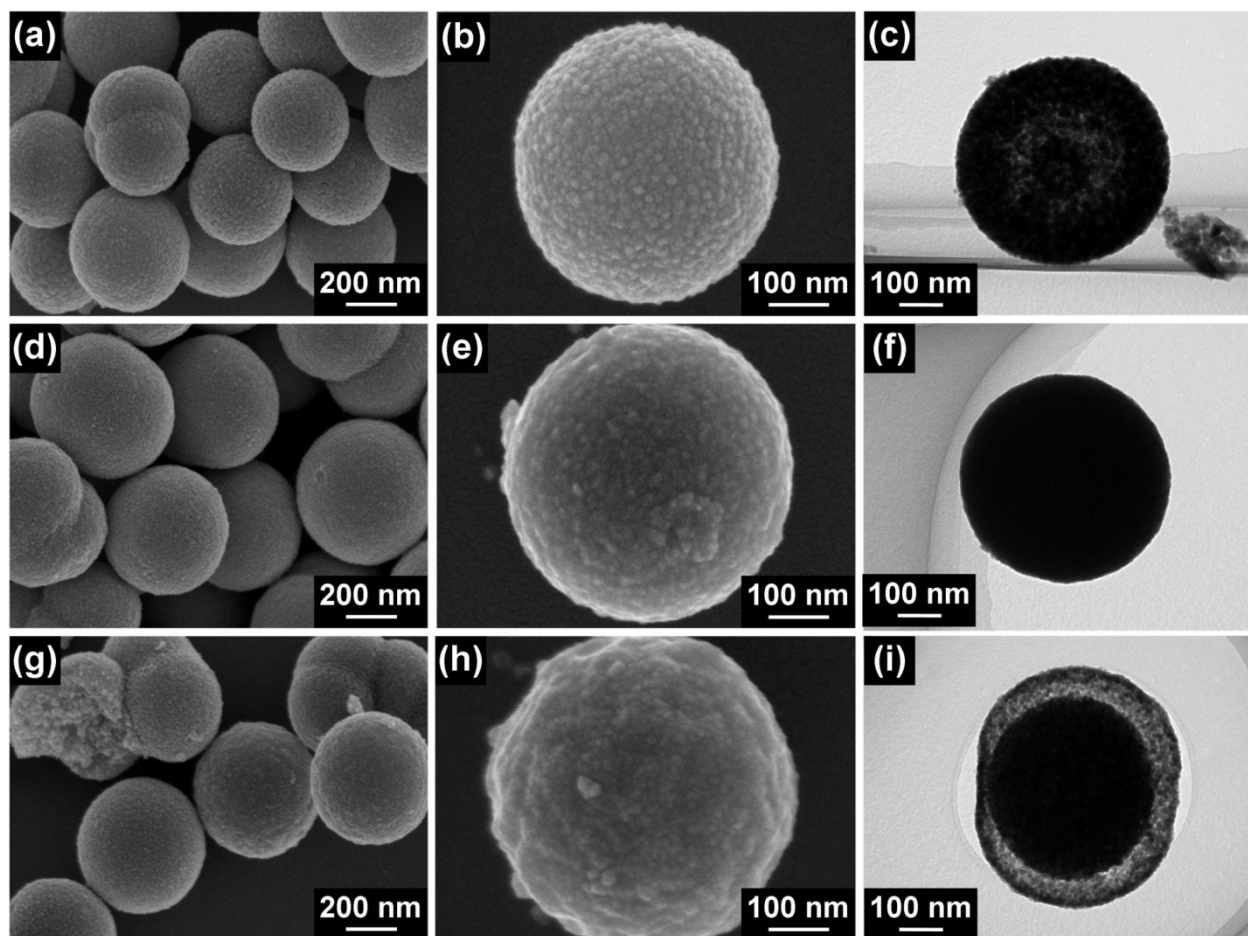


Fig. S2. Low- and high-magnification SEM images and the corresponding TEM images of (a, b, c) Co_3O_4 (d, e, f) NiCo_2O_4 , and (g, h, i) ZnCo_2O_4 nanospheres obtained from the direct calcination of the Co, Ni-Co and Zn-Co glycerate nanospheres, respectively, in air at 350 °C.

SUPPORTING INFORMATION

Comments on Fig. S2:

Fig. S2a and **b** show the low and high-magnification SEM images of the Co_3O_4 nanospheres achieved by direct calcination of the Co-glycerate spheres in air at 350 °C, respectively. The highly uniform spherical morphology of the Co-glycerate precursor is well-preserved after the conversion to Co_3O_4 nanospheres. However, the diameters of these spheres are decreased to 300-500 nm due to the thermal shrinkage resulting from the release of H_2O and CO_2 during calcination (**Fig. S2a**). Furthermore, the surface of the synthesized Co_3O_4 nanospheres is rough, indicating that they are assembled by small nanoparticles, as evident in **Fig. S2b**. The TEM image in **Fig. S2c** reveals that the Co_3O_4 nanospheres exhibit a yolk-shell structure, with the thickness of the shell estimated to be around 100 nm. The shell itself is composed of many small nanocrystals with numerous interparticle pores distributed throughout the shell. In comparison, the synthesized NiCo_2O_4 nanospheres are slightly larger in size with diameters of around 500-700 nm (**Fig. S2d**) and they are also assembled of small nanoparticles, similar to Co_3O_4 (**Fig. S2e**). However, unlike the Co_3O_4 nanospheres, the NiCo_2O_4 nanospheres do not possess a yolk-shell structure, but rather a solid spherical structure (**Fig. S2f**). From **Fig. S2g**, it can be observed that the obtained ZnCo_2O_4 nanospheres exhibit diameters in the range of 500-650 nm and they are also assembled of small nanoparticles with some spheres being partly destroyed due to the large thermal shrinkage (**Fig. S2h**). Based on **Fig. S2i**, it is evident that the ZnCo_2O_4 nanospheres possess a yolk-shell structure, consisting of a solid yolk and a hollow shell. The creation of such a yolk-shell structure may be explained as follows. In the initial heating period during calcination, there exists a high temperature gradient along the radial direction of the solid spheres. This leads to non-homogeneous and non-equilibrium heating, where two opposing forces the cohesive (σ_{co}) and adhesive forces (σ_{ad}) exert at the interface between the ZnCo_2O_4 shell and yolk.¹ If the σ_{co} is larger than σ_{ad} in a large temperature gradient, the inner yolk will separate from the pre-formed shell with continuous heating, leading to the formation of a unique yolk-shell structure.

SUPPORTING INFORMATION

XRD patterns of the metal cobaltite ($M\text{Co}_2\text{O}_4$) nanospheres and 2D nanosheets

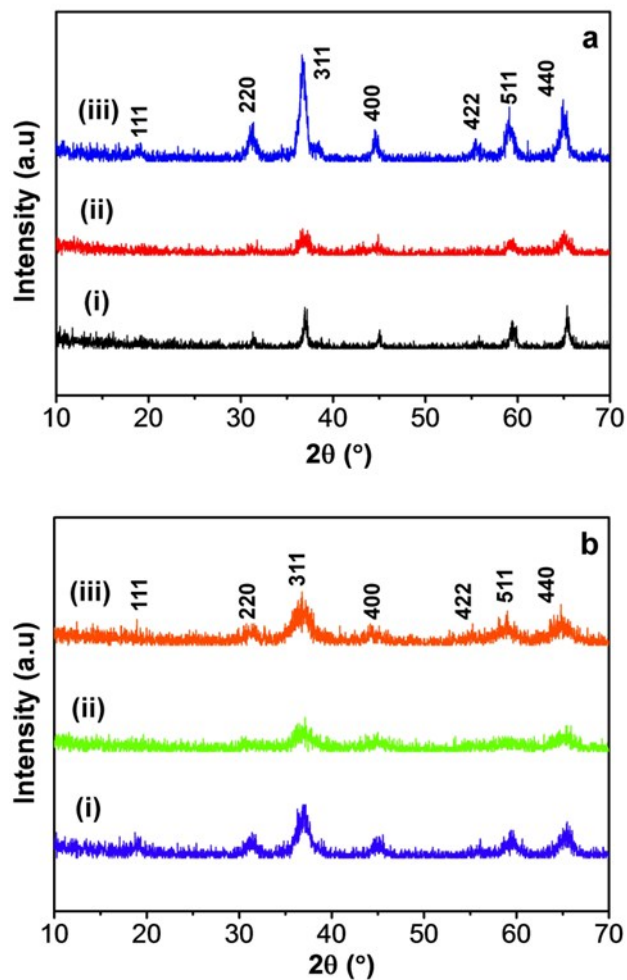


Fig. S3. (a) XRD patterns of (i) Co_3O_4 , (ii) NiCo_2O_4 , and ZnCo_2O_4 nanospheres obtained from the direct calcination of the Co, Ni-Co and Zn-Co glycerate nanospheres, respectively, in air at 350 °C. (b) XRD patterns of (i) Co_3O_4 , (ii) NiCo_2O_4 , and (iii) ZnCo_2O_4 nanosheets achieved by calcination of the Co, Ni-Co and Zn-Co glycerate/hydroxide nanosheets, respectively, in air at 260 °C.

SUPPORTING INFORMATION

EDS mapping of the as-prepared 2D mesoporous metal cobaltite (MCo_2O_4) nanosheets

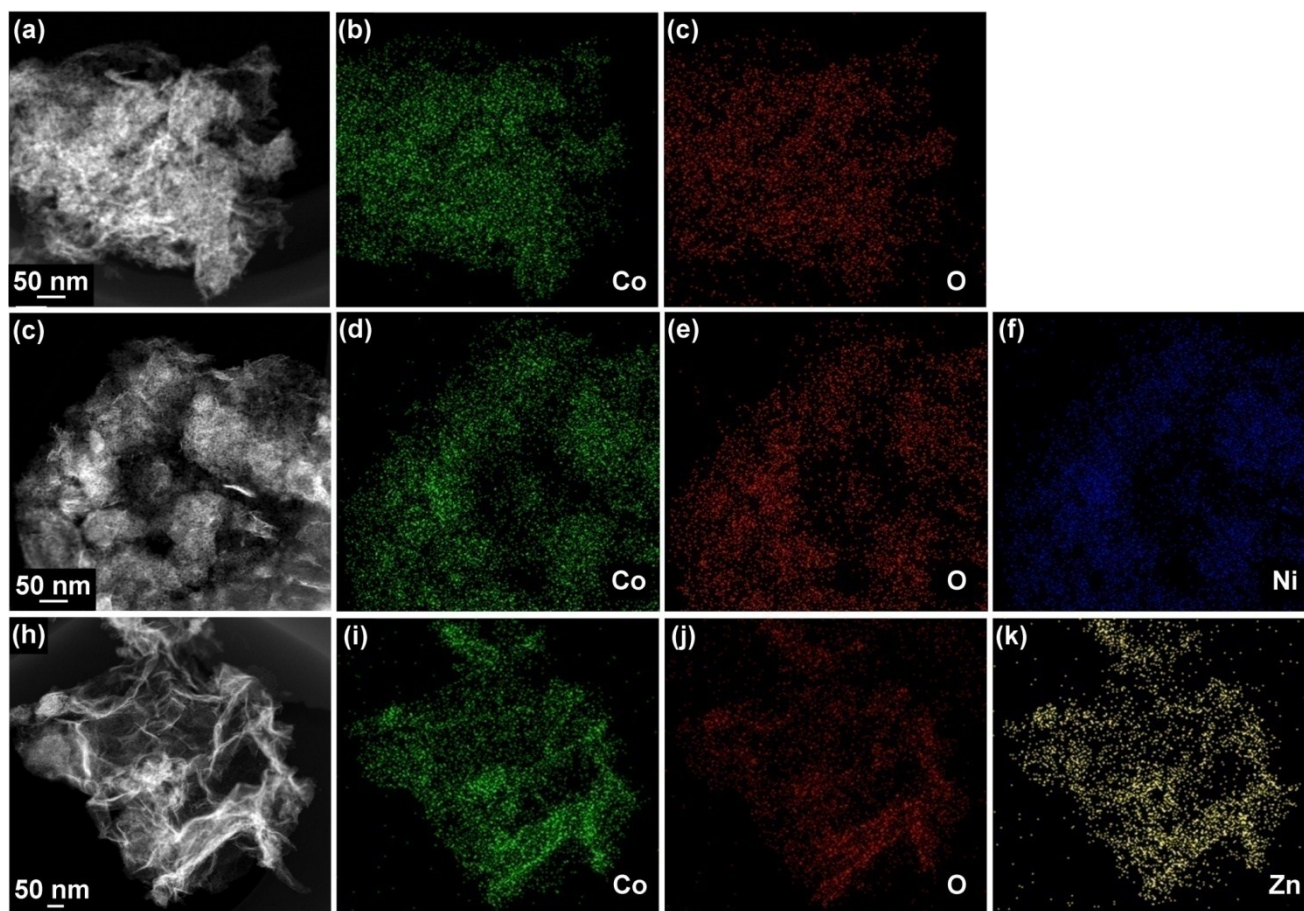


Fig. S4. (a) High-angle annular dark-field scanning transmission electron microscopy (HAADF-STEM) image of a single Co_3O_4 nanosheet and the corresponding elemental mapping for (b) Co and (c) O. (d) HAADF-STEM image of a single $NiCo_2O_4$ nanosheet and the corresponding elemental mapping for (e) Co, (f) O and (g) Ni. (h) HAADF-STEM image of a single $ZnCo_2O_4$ nanosheet and the corresponding elemental mapping for (i) Co, (j) O and (k) Zn.

SUPPORTING INFORMATION

High-magnification TEM and HRTEM images of the 2D mesoporous metal cobaltite ($M\text{Co}_2\text{O}_4$) nanosheets

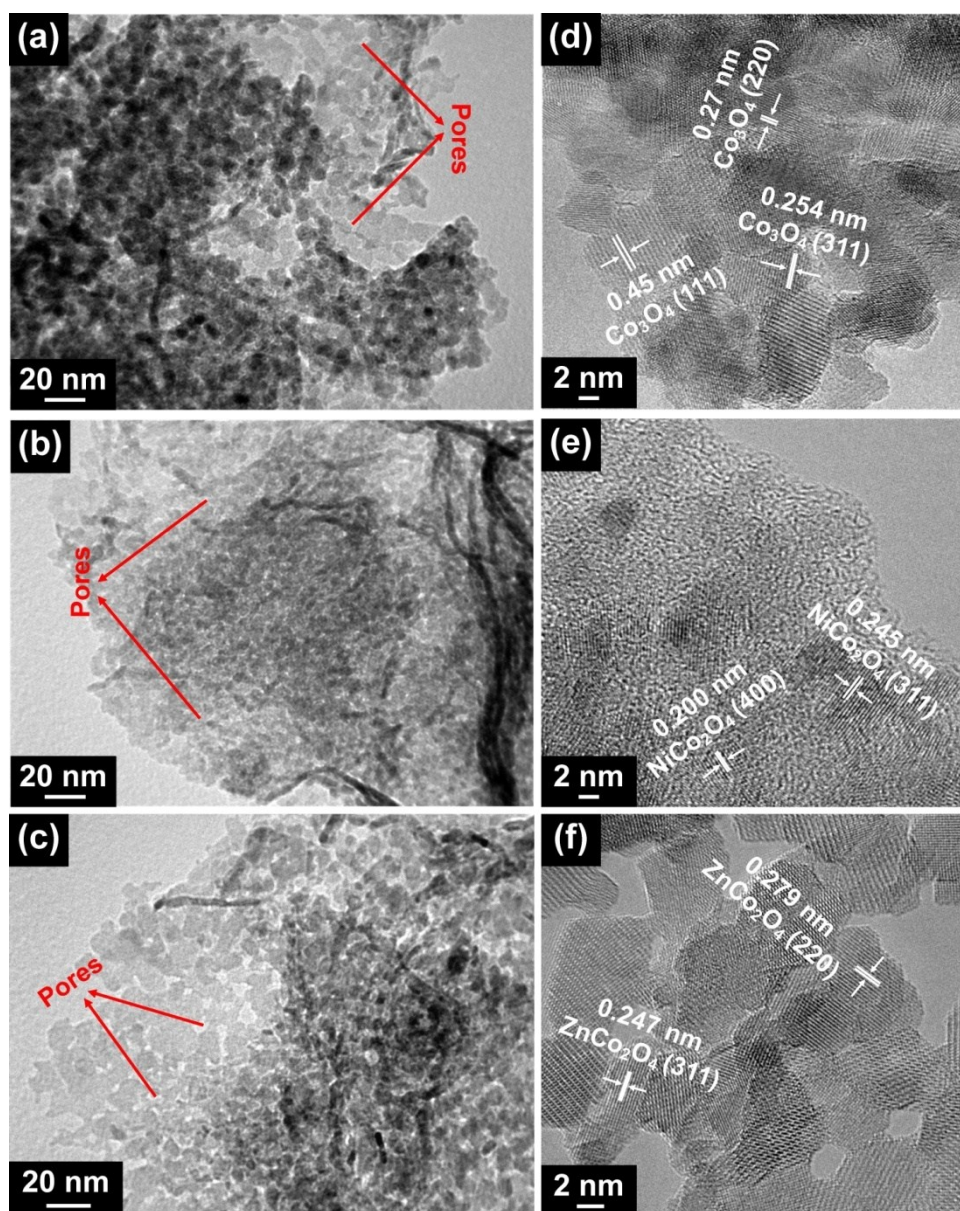


Fig. S5. High-magnification TEM and HRTEM images of the as-prepared 2D mesoporous: Co_3O_4 nanosheets (a, d), NiCo_2O_4 nanosheets (b, e), and ZnCo_2O_4 nanosheets (c, f).

SUPPORTING INFORMATION

N_2 adsorption-desorption isotherms and Barrett-Joyner-Halenda (BJH) pore size distribution curves of the metal cobaltite (MCo_2O_4) nanospheres

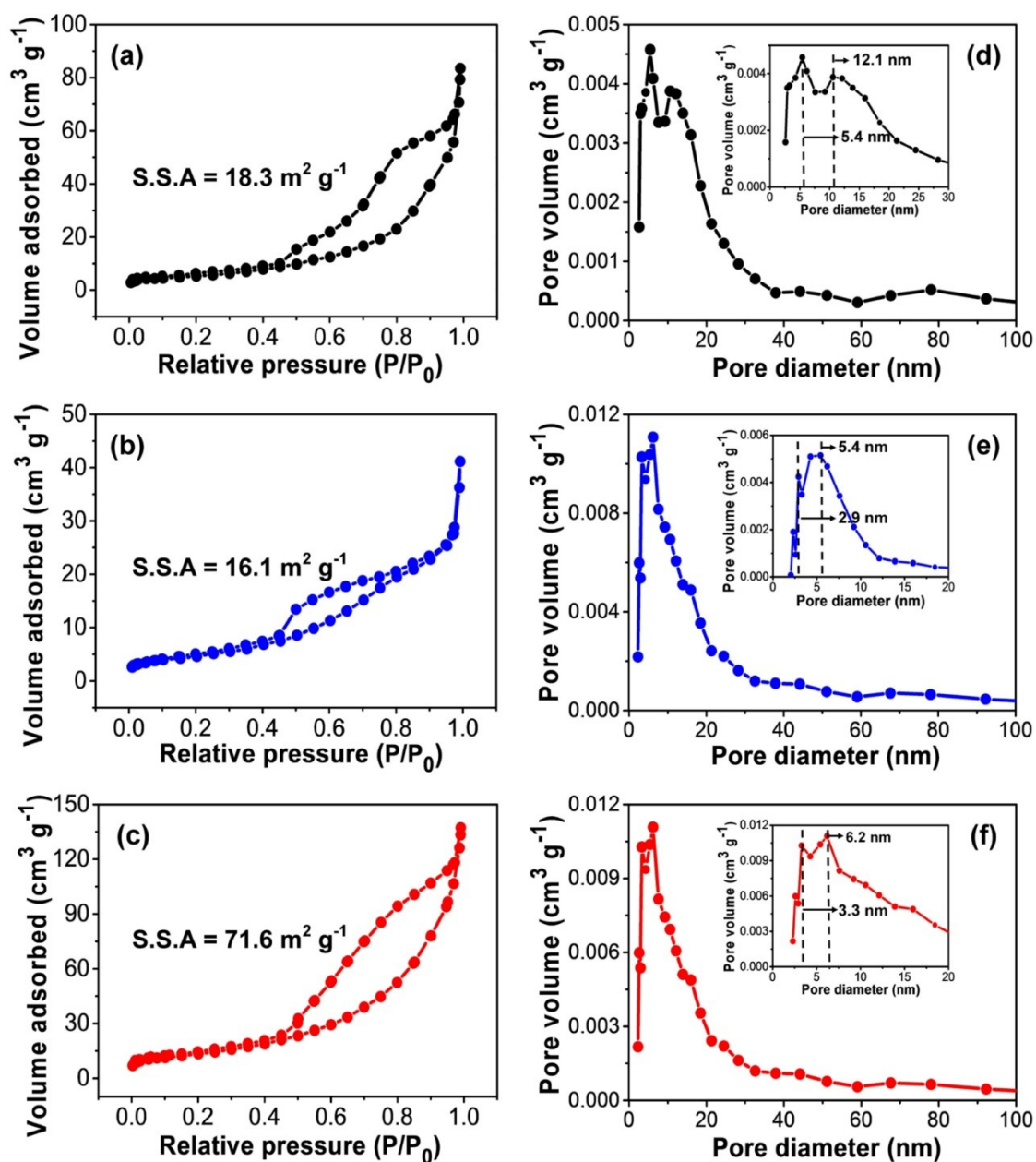


Fig. S6. Nitrogen (N_2) adsorption-desorption isotherms and Barrett-Joyner-Halenda (BJH) pore-size distribution curves of (a, d) Co_3O_4 , (b, e) $NiCo_2O_4$, and (c, f) $ZnCo_2O_4$ nanospheres obtained from the direct calcination of the Co, Ni-Co and Zn-Co glycerate nanospheres, respectively, in air at $350^\circ C$.

SUPPORTING INFORMATION

Comparison of synthetic conditions and textural characteristics of the as-prepared 2D mesoporous metal cobaltite (MCo_2O_4) nanosheets with previous reports

Table S1. Comparison of the synthetic conditions and textural characteristics of the as-prepared 2D mesoporous metal cobaltite nanosheets with previously reported 2D metal cobaltite nanostructures.

| Sample | Synthesis method | Calcination temperature (°) | Surface area ($\text{m}^2 \text{g}^{-1}$) | Pore volume ($\text{cm}^3 \text{g}^{-1}$) | Ref. |
|---|------------------------------------|-----------------------------|---|---|-----------|
| Mesoporous 2D NiCo_2O_4 NSs | Self-deconstruction/reconstruction | 260 | 155 | 0.452 | This work |
| Mesoporous NiCo_2O_4 NSs | Solution-phase | 320 | 113 | N/A | 2 |
| Mesoporous NiCo_2O_4 NSs | Solvothermal | 350 | 124 | 0.203 | 3 |
| Hierarchical NiCo_2O_4 NSs | Solution-phase | 300 | 58.2 | N/A | 4 |
| Hierarchical NiCo_2O_4 NSs | Solvothermal | 250 | 127 | N/A | 5 |
| Mesoporous NiCo_2O_4 NSs | Microwave | 300 | 111 | 0.303 | 6 |
| Ultrathin NiCo_2O_4 NSs | Microwave | 350 | 126 | 0.592 | 7 |
| NiCo_2O_4 NSs | Hydrothermal | 350 | 28.2 | 0.110 | 8 |
| Mesoporous 2D Co_3O_4 NSs | Self-deconstruction/reconstruction | 260 | 175 | 0.785 | This work |
| Porous Co_3O_4 NSs | Hydrothermal | 300 | 69.7 | N/A | 9 |
| Porous Co_3O_4 NSs | Topological transformation | 600 | 87.0 | 0.235 | 10 |
| Ultrathin Co_3O_4 NSs | Hydrothermal | 300 | 68.7 | N/A | 11 |
| Mesoporous Co_3O_4 NSs | Electrodeposition | 250 | 56.1 | N/A | 12 |
| Mesoporous Co_3O_4 NSs | Chemical co-precipitation | 450 | 29.4 | 0.335 | 13 |
| Mesoporous 2D ZnCo_2O_4 NSs | Self-deconstruction/reconstruction | 260 | 171 | 0.867 | This work |
| Mesoporous ZnCo_2O_4 NSs | Hydrothermal | 350 | 63.4 | N/A | 14 |

Note: NSs= nanosheets

SUPPORTING INFORMATION

Comparison of Co 2p, Ni 2p, and Zn 2p XPS binding energies of the as-prepared 2D mesoporous metal cobaltite (MCo₂O₄) nanosheets with previous literatures

Table S2. Binding energy values of Co 2p, Ni 2p, and Zn 2p peaks for metal cobaltites found in literatures.

| Ref. | Sample | BE (Co2p _{3/2}) (eV) | BE (Co2p _{1/2}) (eV) | BE (Ni2p _{3/2}) (eV) | BE (Ni2p _{1/2}) (eV) | BE (Zn2p _{3/2}) (eV) | BE (Zn2p _{1/2}) (eV) |
|-----------|--------------------------------------|-----------------------------------|-----------------------------------|-----------------------------------|-----------------------------------|-----------------------------------|-----------------------------------|
| This work | NiCo ₂ O ₄ NSs | 781.8 (Co ²⁺) | 797.1 (Co ²⁺) | 854.2 (Ni ²⁺) | 871.8 (Ni ²⁺) | - | - |
| | | 780.1 (Co ³⁺) | 795.2 (Co ³⁺) | 855.8 (Ni ³⁺) | 873.3 (Ni ³⁺) | | |
| 15 | NiCo ₂ O ₄ NWs | 780.8 (Co ²⁺) | 795.8 (Co ²⁺) | 854.1 (Ni ²⁺) | 871.9 (Ni ²⁺) | - | - |
| | | 779.4 (Co ³⁺) | 794.7 (Co ³⁺) | 855.8 (Ni ³⁺) | 873.6 (Ni ³⁺) | | |
| 16 | NiCo ₂ O ₄ NRs | 781.0 (Co ²⁺) | 796.4 (Co ²⁺) | 854.1 (Ni ²⁺) | 871.9 (Ni ²⁺) | - | - |
| | | 779.3 (Co ³⁺) | 794.5 (Co ³⁺) | 855.8 (Ni ³⁺) | 873.8 (Ni ³⁺) | | |
| This work | Co ₃ O ₄ NSs | 781.0 (Co ²⁺) | 796.4 (Co ²⁺) | - | - | - | - |
| | | 779.3 (Co ³⁺) | 794.5 (Co ³⁺) | | | | |
| 17 | Co ₃ O ₄ | 781.4 (Co ²⁺) | 796.9 (Co ²⁺) | - | - | - | - |
| | | 779.2 (Co ³⁺) | 794.3 (Co ³⁺) | | | | |
| 18 | Co ₃ O ₄ NPs | 781.4 (Co ²⁺) | 796.8 (Co ²⁺) | - | - | - | - |
| | | 779.7 (Co ³⁺) | 794.8 (Co ³⁺) | | | | |
| This work | ZnCo ₂ O ₄ NSs | 781.4 (Co ²⁺) | 796.8 (Co ²⁺) | - | - | 1021.2 (Zn ²⁺) | 1044.5 (Zn ²⁺) |
| | | 780.2 (Co ³⁺) | 795.2 (Co ³⁺) | | | | |
| 16 | ZnCo ₂ O ₄ NRs | 781.0 (Co ²⁺) | 796.4 (Co ²⁺) | - | - | - | - |
| | | 780.1 (Co ³⁺) | 795.5 (Co ³⁺) | | | | |
| 19 | ZnCo ₂ O ₄ NFs | 780.2 (Co ³⁺) | 794.5 (Co ³⁺) | - | - | 1022.5 (Zn ²⁺) | 1045.7 (Zn ²⁺) |

Notes: NSs= nanosheets; NWs= nanowires; NFs= nanofibers; NPs= nanoparticles; NRs= nanorods

SUPPORTING INFORMATION

Comparison of the electrochemical performance of the metal cobaltite (MCo_2O_4) nanospheres with the 2D mesoporous MCo_2O_4 nanosheets

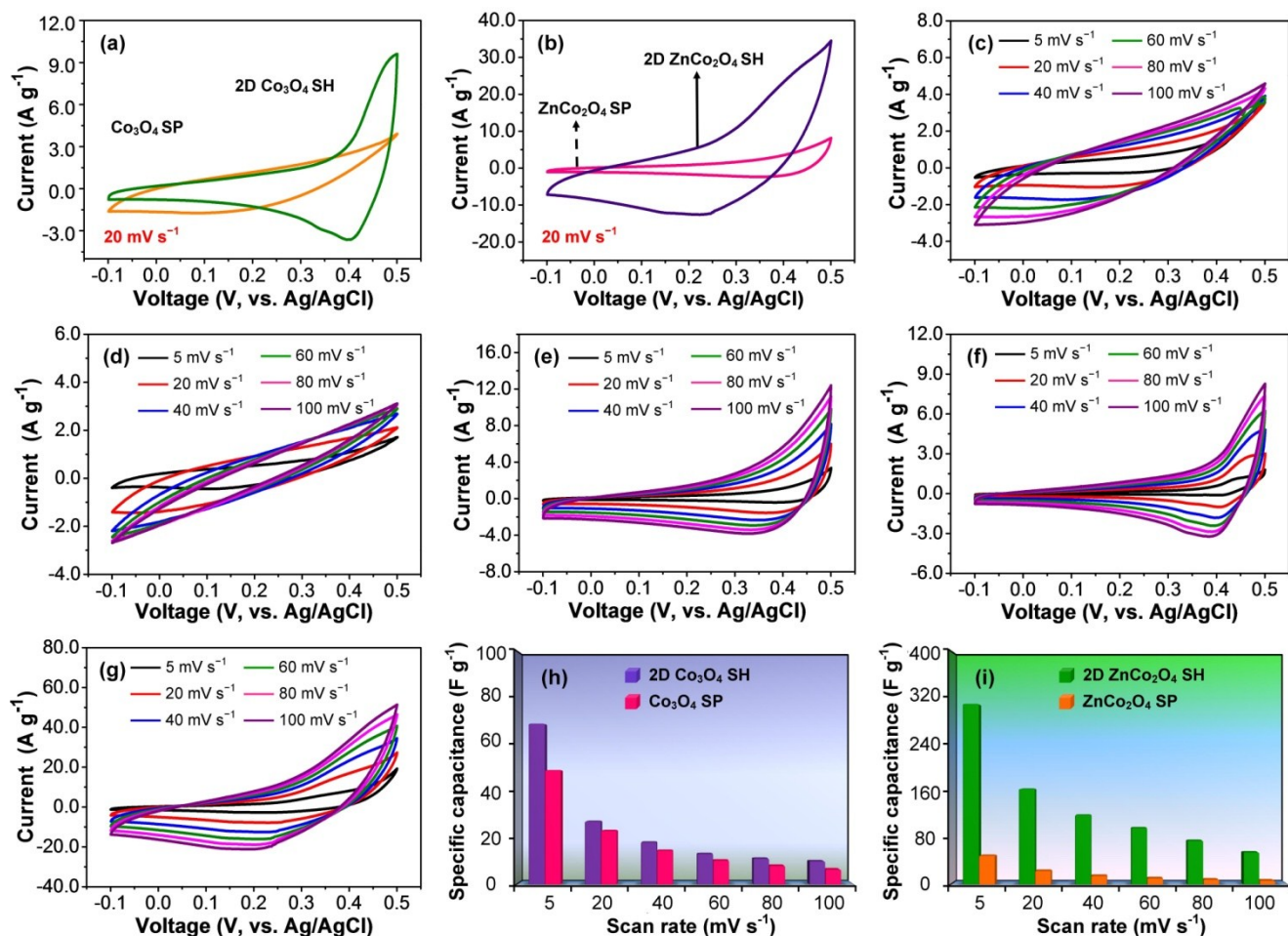


Fig. S7. Comparison of CV curves between (a) Co_3O_4 nanospheres and 2D mesoporous Co_3O_4 nanosheets and (b) ZnCo_2O_4 nanospheres and 2D mesoporous ZnCo_2O_4 nanosheets at a fixed scan rate of 20 mV s^{-1} . CV curves of (c) Co_3O_4 nanospheres, (d) NiCo_2O_4 nanospheres, (e) ZnCo_2O_4 nanospheres, (f) 2D mesoporous Co_3O_4 nanosheets, and (g) 2D mesoporous ZnCo_2O_4 nanosheets at various scan rates from 5-100 mV s^{-1} . (h) Scan rate dependence of specific capacitance for porous Co_3O_4 nanospheres and 2D mesoporous Co_3O_4 nanosheets. (i) Scan rate dependence of specific capacitance for ZnCo_2O_4 nanospheres and 2D mesoporous ZnCo_2O_4 nanosheets.

SUPPORTING INFORMATION

Comments on Fig. S7:

Fig. S7a and b compare the CV curves of the Co_3O_4 nanospheres and 2D mesoporous Co_3O_4 nanosheets and CV curves of the ZnCo_2O_4 nanospheres and 2D mesoporous ZnCo_2O_4 nanosheets, respectively, at a fixed scan rate of 20 mV s^{-1} . Evidently, both 2D mesoporous Co_3O_4 and ZnCo_2O_4 nanosheets exhibit higher current densities and CV curve areas than their spherical counterparts, thus indicating their higher electrochemical activities. The CV curves of the Co_3O_4 and NiCo_2O_4 nanospheres at all scan rates do not show clear presence of the redox peaks (**Fig. S7c and d**), suggesting their poor electrochemical activities, which may be due to the kinetically slow surface reactions contributed by the low surface area ($10\text{-}20 \text{ m}^2 \text{ g}^{-1}$) and small pore volume ($0.057\text{-}0.127 \text{ cm}^3 \text{ g}^{-1}$).²⁰ In contrast, the CV curve of the ZnCo_2O_4 nanospheres show the existence of redox peaks at a scan rate of 5 mV s^{-1} , which originate from the reversible Faradaic redox reactions related to M-O/M-O-OH (M refers to Co and Zn ions) associated with OH^- anions, thus indicating their pseudocapacitive characteristics (**Fig. S7e**).²¹ The cathodic peak is shifted to lower potential with increasing scan rate, while the anodic peak is shifted to higher potential, but the potential window is not wide enough to show this shift. **Fig. S7f** depicts the CV curves of the 2D mesoporous Co_3O_4 nanosheets at various scan rates from 5 to 100 mV s^{-1} . At a low scan rate (5 mV s^{-1}), a pair of redox peaks can be observed from the CV curve of the mesoporous Co_3O_4 nanosheets which indicates their pseudocapacitive behavior. The presence of this pair of redox peaks can be attributed to the Faradaic redox reactions of Co_3O_4 in the KOH electrolyte based on the following equations²².



The increase in scan rate does not affect the shape of the CV curves significantly, but simply shifts the cathodic peak to lower potential, as a result of the polarization of the electrode at higher scan rates.¹⁷ At higher scan rates, the voltage window is not wide enough to show the shift of the anodic peak to higher potential. The CV curves of the 2D ZnCo_2O_4 nanosheets are depicted in **Fig. S7g**. These curves show a similar trend as that of NiCo_2O_4 nanosheets. From **Fig. S7h**, it can be observed that the 2D mesoporous Co_3O_4 nanosheets exhibit specific capacitances of 69.0, 27.0, 18.0, 13.0, 11.0, 10.0 F g^{-1} at scan rates of 5, 20, 40, 60, 80, and 100 mV s^{-1} , respectively. Comparatively, the Co_3O_4 nanospheres display specific capacitances of 40.0, 19.0, 15.0, 13.0, 12.0, and 11.0 F g^{-1} , respectively. Moreover, the specific capacitances of the 2D ZnCo_2O_4 nanosheets are 310, 164, 119, 97, 75, and 55 F g^{-1} at scan rates of 5, 20, 40, 60, 80 and 100 mV s^{-1} , respectively, as shown in **Fig. S7i**. In comparison, the specific capacitances of the ZnCo_2O_4 nanospheres are 37.0, 21.0, 16.0, 14.0, 12.0, and 11.0 F g^{-1} , respectively, which are considerably lower (5-10 times lower) than those of the 2D mesoporous ZnCo_2O_4 nanosheets.

SUPPORTING INFORMATION

These results indicate the superior electrochemical performance of the 2D mesoporous metal cobaltite nanosheets relative to the metal cobaltite nanospheres. Compared to NiCo_2O_4 , the 2D mesoporous ZnCo_2O_4 nanosheets display higher specific capacitance at lower scan rates; however the specific capacitance fades much more rapidly with a relatively low retention rate of 38% with the increase in scan rate from 5 to 40 mV s^{-1} (**Fig. S7i**), while the 2D mesoporous Co_3O_4 nanosheets show the lowest capacitive performance among the three samples (**Fig. S7h**). This is because of the richer redox reactions (contributed by both Co^{2+} and $\text{Ni}^{2+}/\text{Zn}^{2+}$ ions) and higher electronic conductivity of MCo_2O_4 compared to Co_3O_4 by several order of magnitudes.²³

SUPPORTING INFORMATION

Comparison of the electrochemical performance of the assembled 2D NiCo₂O₄ nanosheets//GO asymmetric supercapacitor (ASC) with previously reported ASCs

Table S3. Comparison of the electrochemical performance of the assembled 2D NiCo₂O₄ nanosheets//GO asymmetric supercapacitor (ASC) with previously reported ASCs.

| ASC | Electrolyte | Operating voltage (V) | Energy density (W h kg ⁻¹) | Power density (W kg ⁻¹) | Cycling Performance (retention) | Ref |
|---|-------------|-----------------------|--|-------------------------------------|---|-----------|
| 2D NiCo ₂ O ₄ NSs//GO | 3 M KOH | 1.6 | 38.5 | 299 | 91% after 2000 cycles at 5 A g ⁻¹ | This work |
| Porous NiCo ₂ O ₄ //AC | 1 M KOH | 1.4 | 14.7 | 175 | 85% after 5000 cycles at 1.5 A g ⁻¹ | 24 |
| Mesoporous NiCo ₂ O ₄ //AC | 6 M KOH | 1.6 | 29.8 | 159.4 | 103% after 5000 cycles at 2 A g ⁻¹ | 25 |
| Hierarchical NiCo ₂ O ₄ //AC | 2 M KOH | 1.4 | 21.4 | 350 | 95.6% after 1000 cycles at 1 A g ⁻¹ | 26 |
| NiCo ₂ O ₄ NSs-CNTs//AC | 6 M KOH | 1.25 | 19.8 | ~150 | ~100% after 1000 cycles at 2 A g ⁻¹ | 27 |
| NiCo ₂ O ₄ spheres-CQDs//AC | 2 M KOH | 1.5 | 29.0 | ~125 | 101.9% after 5000 cycles at 3 A g ⁻¹ | 28 |
| NiCo ₂ O ₄ -RGO//AC | 2 M KOH | 1.3 | 23.3 | 324.9 | 83% after 2500 cycles at 2 A g ⁻¹ | 29 |
| NiCo ₂ O ₄ -MnO ₂ //AG | 2 M KOH | 1.6 | 9.40 | ~180 | 89.7% after 3000 cycles at 5 A g ⁻¹ | 30 |
| NiCo ₂ O ₄ -GO//AC | 6 M KOH | 1.4 | 19.5 | ~120 | ~97% after 10000 cycles at 10 A g ⁻¹ | 31 |
| ZnCo ₂ O ₄ MS//AC | PVA/KOH gel | 1.4 | 22.0 | ~39.0 | 76.68% after 1000 cycles at 0.5 A g ⁻¹ | 20 |
| ZnCo ₂ O ₄ NWs//AC | 6 M KOH | 1.5 | 35.6 | 187.6 | 94% after 3000 cycles at 3 A g ⁻¹ | 32 |
| Co ₃ O ₄ NSs-RGO//AC | 2 M KOH | 1.45 | 13.4 | ~200 | 89% after 1000 cycles at 1 A g ⁻¹ | 33 |
| FeCo ₂ O ₄ NWs//AC | 3 M KOH | 1.5 | 23.0 | 236 | 97% after 1500 cycles at 40 mV s ⁻¹ | 34 |
| NiO nanopetals//AC | 2 M KOH | 1.7 | 14.6 | 118 | 91.3% after 10000 cycles at 1 A g ⁻¹ | 35 |

Notes: NSs= nanosheets; MS= microspheres; NWs= nanowires; AC= activated carbon; AG= activated graphene; GO= graphene oxide; RGO= reduced graphene oxide; CNTs= carbon nanotubes; CQDs= carbon quantum dots.

SUPPORTING INFORMATION

Additional electrochemical data of the assembled 2D NiCo₂O₄ nanosheets//GO ASC

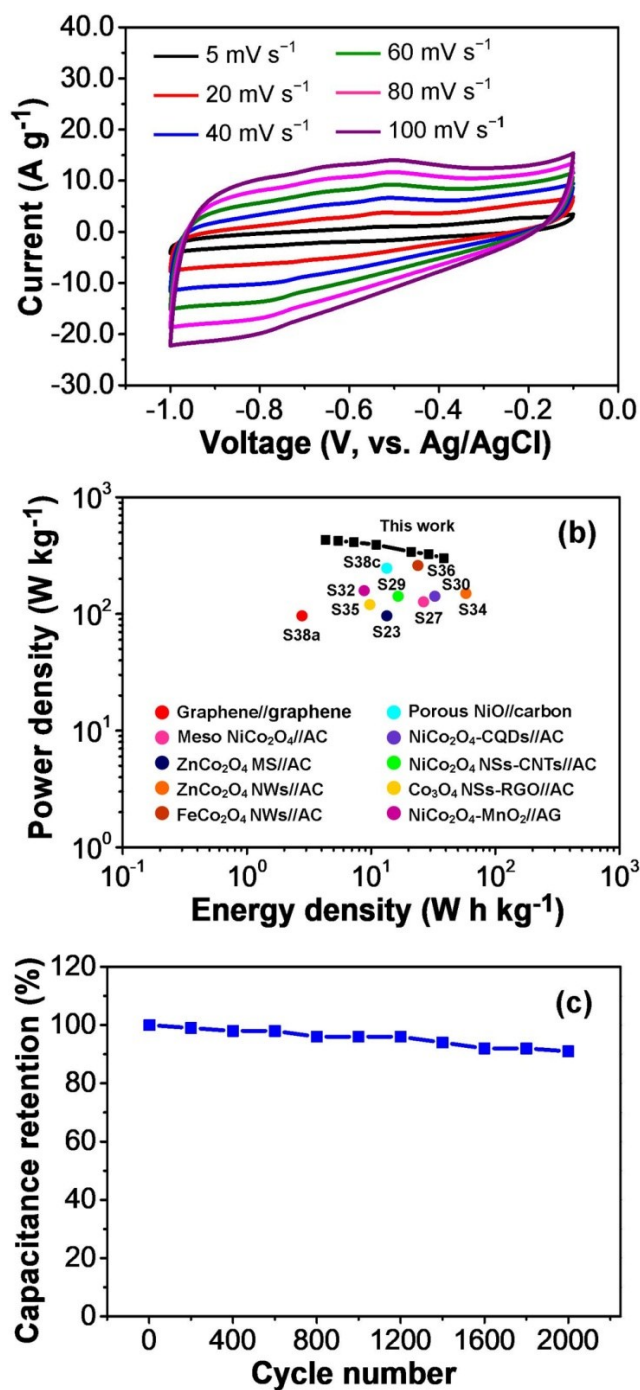


Fig. S8. (a) CV curves of the graphene oxide (GO) electrode at various scan rates from 5-100 mV s⁻¹. (b) Comparison of the electrochemical performance of the assembled NiCo₂O₄ nanosheets//GO ASC with previously reported ASCs based on metal cobaltites and carbon materials. (c) Cycling performance of the assembled 2D NiCo₂O₄ nanosheets//GO ASC during 2000 cycles at a current density of 5 A g⁻¹.

SUPPORTING INFORMATION

Comments on Fig. S8:

Fig. S8a displays the CV curves of the graphene oxide (GO) electrode at various scan rates ranging from 5 to 100 mV s^{-1} within the potential window of -1.0 to -0.1 V vs. Ag/AgCl. The quasi-rectangular shape of the CV curves indicates the electrical double-layer capacitive behaviour of the GO electrode. The area of the CV curve increases with increasing scan rate, which suggests good reversibility and rate capability.³⁶⁻³⁸ The corresponding specific capacitance values of the GO electrode are 118, 80, 68, 63, 59, and 56 F g^{-1} at scan rates of 5, 20, 40, 60, 80 and 100 mV s^{-1} , respectively (**Fig. 8c**), corresponding to a capacitance retention of 47.4% which is considerably lower than the value obtained for 2D mesoporous NiCo_2O_4 nanosheets.

SUPPORTING INFORMATION

SEM images of the NiCo₂O₄ nanosheet electrode after cycling

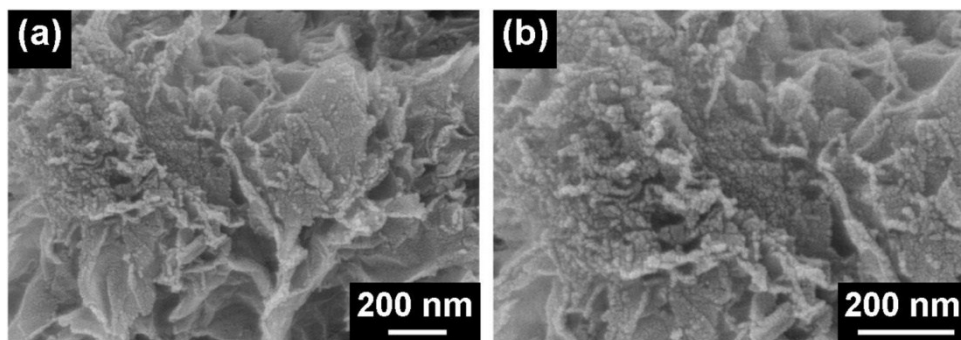


Fig. S9. (a) Low and (b) high-magnification SEM images of the NiCo₂O₄ nanosheet electrode after 2000 cycles at 5 A g⁻¹.

SUPPORTING INFORMATION

References

1. J. Li, J. Wang, X. Liang, Z. Zhang, H. Liu, Y. Qian and S. Xiong, *ACS Appl. Mater. Interfaces*, 2014, **6**, 24-30.
2. G. Zhang and X. W. Lou, *Adv. Mater.*, 2013, **25**, 976-979.
3. C.-T. Hsu and C.-C. Hu, *J. Power Sources*, 2013, **242**, 662-671.
4. G. Gao, H. B. Wu, S. Ding, L.-M. Liu and X. W. Lou, *Small*, 2015, **11**, 804-808.
5. B. Sun, X. Huang, S. Chen, Y. Zhao, J. Zhang, P. Munroe and G. Wang, *J. Mater. Chem. A*, 2014, **2**, 12053-12059.
6. S. Khalid, C. Cao, A. Ahmad, L. Wang, M. Tanveer, I. Aslam, M. Tahir, F. Idrees and Y. Zhu, *RSC Adv.*, 2015, **5**, 33146-33154.
7. Y. Zhu and C. Cao, *Electrochim. Acta*, 2015, **176**, 141-148.
8. H. Wang and X. Wang, *ACS Appl. Mater. Interfaces*, 2013, **5**, 6255-6260.
9. F. Zhan, B. Geng and Y. Guo, *Chem. Eur. J.*, 2009, **15**, 6169-6174.
10. J. Zhu, L. Bai, Y. Sun, X. Zhang, Q. Li, B. Cao, W. Yan and Y. Xie, *Nanoscale*, 2013, **5**, 5241-5246.
11. Z. Zhang, Z. Wen, Z. Ye and L. Zhu, *RSC Adv.*, 2015, **5**, 59976-59982.
12. Y. Zheng, W. Wang, D. Jiang, L. Zhang, X. Li and Z. Wang, *J. Mater. Chem. A*, 2016, **4**, 105-112.
13. S. Deng, X. Liu, N. Chen, D. Deng, X. Xiao and Y. Wang, *Sens. Actuator B*, 2016, **233**, 615-623.
14. F. Bao, X. Wang, X. Zhao, Y. Wang, Y. Ji, H. Zhang and X. Liu, *RSC Adv.*, 2014, **4**, 2393-2397.
15. J. Wang, S. Fan, Y. Luan, J. Tang, Z. Jin, M. Yang and Y. Lu, *RSC Adv.*, 2015, **5**, 2405-2410.
16. S. G. Mohamed, Y.-Q. Tsai, C.-J. Chen, Y.-T. Tsai, T.-F. Hung, W.-S. Chang and R.-S. Liu, *ACS Appl. Mater. Interfaces*, 2015, **7**, 12038-12046.
17. C. Zhang, J. Xiao, X. Lv, L. Qian, S. Yuan, S. Wang and P. Lei, *J. Mater. Chem. A*, 2016, **4**, 16516-16523.
18. W. Guo, Y. E, I. Gao, L. Fan and S. Yang, *Chem. Commun.*, 2010, **46**, 1290-1292.
19. W. Luo, X. Hu, Y. Sun and Y. Huang, *J. Mater. Chem.*, 2012, **22**, 8916-8921.
20. Y. Gai, Y. Shang, L. Gong, L. Su, L. Hao, F. Dong and J. Li, *RSC Adv.*, 2017, **7**, 1038-1044.
21. G. Q. Zhang, H. B. Wu, H. E. Hoster, M. B. Chan-Park and X. W. Lou, *Energy Environ. Sci.*, 2012, **5**, 9453-9456.
22. X. Zhou, X. Shen, Z. Xia, Z. Zhang, J. Li, Y. Ma and Y. Qu, *ACS Appl. Mater. Interfaces*, 2015, **7**, 20322-20331.
23. C. Yuan, H. B. Wu, Y. Xie and X. W. Lou, *Angew. Chem. Int. Ed.*, 2014, **53**, 1488-1504.
24. R. Ding, L. Qi, M. Jia and H. Wang, *Electrochim. Acta*, 2013, **107**, 494-502.

SUPPORTING INFORMATION

25. M. J. Pang, S. Jiang, G. H. Long, Y. Ji, W. Han, B. Wang, X. L. Liu, Y. L. Xi, F. Z. Xu and G. D. Wei, *RSC Adv.*, 2016, **6**, 67839-67848.
26. S. Wang, S. Sun, S. Li, F. Gong, Y. Li, Q. Wu, P. Song, S. Fang and P. Wang, *Dalton Trans.*, 2016, **45**, 7469-7475.
27. F. Cai, Y. Kang, H. Chen, M. Chen and Q. Li, *J. Mater. Chem. A*, 2014, **2**, 11509-11515.
28. Y. Zhu, Z. Wu, M. Jing, H. Hou, Y. Yang, Y. Zhang, X. Yang, W. Song, X. Jia and X. Ji, *J. Mater. Chem. A*, 2015, **3**, 866-877.
29. X. Wang, W. S. Liu, X. Lu and P. S. Lee, *J. Mater. Chem.*, 2012, **22**, 23114-23119.
30. M. Kuang, Z. Q. Wen, X. L. Guo, S. M. Zhang and Y. X. Zhang, *J. Power Sources*, 2014, **270**, 426-433.
31. H. Wang, C. M. B. Holt, Z. Li, X. Tan, B. S. Amirkhiz, Z. Xu, B. C. Olsen, T. Stephenson and D. Mitlin, *Nano Res.*, 2012, **5**, 605-617.
32. C. Wu, J. Cai, Q. Zhang, X. Zhou, Y. Zhu, P. K. Shen and K. Zhang, *ACS Appl. Mater. Interfaces*, 2015, **7**, 26512-26521.
33. C. Yuan, L. Zhang, L. Hou, G. Pang and W.-C. Oh, *RSC Adv.*, 2014, **4**, 14408-14413.
34. A. Pendashteh, J. Palma, M. Anderson and R. Marcilla, *J. Mater. Chem. A*, 2015, **3**, 16849-16859.
35. G. Cheng, Q. Bai, C. Si, W. Yang, C. Dong, H. Wang, Y. Gao and Z. Zhang, *RSC Adv.*, 2015, **5**, 15042-15051.
36. S. Khalid, C. Cao, L. Wang and Y. Zhu, *Sci. Rep.*, 2016, **6**, 22699.
37. R. R. Salunkhe, J. Tang, Y. Kamachi, T. Nakato, J. H. Kim and Y. Yamauchi, *ACS Nano*, 2015, **9**, 6288-6296.
38. D.-W. Wang, F. Li and H.-M. Cheng, *J. Power Sources*, 2008, **185**, 1563-1568.